

Unraveling the Intra and Intercycle Interfacial Evolution of $\text{Li}_6\text{PS}_5\text{Cl}$ -Based All-Solid-State Lithium Batteries

Jun Zhang, Chao Zheng, Lujie Li, Yang Xia, Hui Huang, Yongping Gan, Chu Liang, Xinping He, Xinyong Tao, and Wenkui Zhang*

High-performance rechargeable all-solid-state lithium metal batteries with high energy density and enhanced safety are attractive for applications like portable electronic devices and electric vehicles. Among the various solid electrolytes, argyrodite $\text{Li}_6\text{PS}_5\text{Cl}$ with high ionic conductivity and easy processability is of great interest. However, the low interface compatibility between sulfide solid electrolytes and high capacity cathodes like nickel-rich layered oxides requires many thorny issues to be resolved, such as the space charge layer (SCL) and interfacial reactions. In this work, in situ electrochemical impedance spectroscopy and in situ Raman spectroscopy measurements are performed to monitor the detailed interface evolutions in a $\text{LiNi}_{0.8}\text{Co}_{0.1}\text{Mn}_{0.1}\text{O}_2$ (NCM)/ $\text{Li}_6\text{PS}_5\text{Cl}$ /Li cell. Combining with ex situ characterizations including scanning electron microscopy and X-ray photoelectron spectroscopy, the evolution of the SCL and the chemical bond vibration at NCM/ $\text{Li}_6\text{PS}_5\text{Cl}$ interface during the early cycles is elaborated. It is found that the Li^+ ion migration, which varies with the potential change, is a very significant cause of these interface behaviors. For the long-term cycling, the SCL, interfacial reactions, lithium dendrites, and chemo-mechanical failure have an integrated effect on interfaces, further deteriorating the interfacial structure and electrochemical performance. This research provides a new insight on intra and intercycle interfacial evolution of solid-state batteries.

1. Introduction

Lithium-ion batteries (LIBs) have been widely used in energy storage systems.^[1] However, there are added safety risks in the use of large LIBs for grid-scale storage and transport application, as organic liquid electrolytes (LEs) in LIBs are volatile and flammable.^[1c,2] Moreover, when using metallic lithium as anode to achieve higher energy density, LEs are facing dangerous battery failure triggered by lithium dendrite growth. To solve these issues, replacing the commonly used LEs in LIBs with solid electrolytes (SEs) to achieve all-solid-state lithium


batteries (ASSLBs) has unique benefits including higher degree of safety and higher energy density. Early researches focus on the design and synthesis of SEs with high ionic conductivity, which has been dramatically improved over the past few years.^[3] Ionic conductivity that is comparable to LEs ($>10^{-3} \text{ S cm}^{-1}$) has been achieved in several inorganic SEs, suggesting the bright future of ASSLBs.

Among various SEs materials, sulfide-type SEs stand out by high ionic conductivity, low grain boundary resistance, and easy processability.^[3d,4] According to their chemical compositions, all known sulfide-type SEs are divided into thiophosphates,^[5] halide thiophosphates,^[6] glassy sulfides electrolytes,^[7] and sulfide without phosphorus.^[8] In these categories, many works are based on Li_3PS_4 and $\text{Li}_7\text{P}_3\text{S}_{11}$. Comparing with Li_3PS_4 , $\text{Li}_7\text{P}_3\text{S}_{11}$ has higher ionic conductivity ($3.2 \times 10^{-3} \text{ S cm}^{-1}$) and lower activation energy (12 kJ mol^{-1}).^[5b] Its framework is composed of the PS_4 tetrahedra and P_2S_7 ditetrahedron.^[9] Another high ionic conductive solid electrolyte $\text{Li}_{10}\text{GeP}_2\text{S}_{12}$ (LGPS) shows a new

framework composing of $(\text{Ge}_{0.5}\text{P}_{0.5})\text{S}_4$, PS_4 , and LiS_4 tetrahedra and LiS_6 octahedra.^[4,5c] The sulfide-type SEs with halogen elements have very similar frameworks but wider electrochemical windows.^[6b,10] Among these SEs, Li-argyrodite $\text{Li}_6\text{PS}_5\text{Cl}$ has an attractive prospect, because of its easy processability, high thermostability, high ionic conductivity ($1.3 \times 10^{-3} \text{ S cm}^{-1}$), and wide electrochemical window (up to above 7 V vs Li^+).^[6a,11] And $\text{Li}_6\text{PS}_5\text{X}$ ($\text{X} = \text{Cl}, \text{Br}, \text{I}$) is also constructed of PS_4 tetrahedra, which are all connected via interstitial site around halide ions and resulted in the ionic formula $(\text{Li}^+)_6(\text{PS}_4^{3-})\text{S}^{2-}\text{X}^-$.^[10,12] This ionic formula is similar to the corresponding Ag and Cu argyrodites.^[13]

All these sulfide-type SEs, in spite of their benefits, are not universally applied in energy storage systems. Most of the ASSLBs with high ionic conductivity sulfide-type SEs cannot be the substitute for their liquid counterparts yet, because of their uncompetitive electrochemical performance (including specific capacity, initial Coulombic efficiency, and capacity retention rate). There are a number of problems such as space charge layer (SCL),^[14] interfacial reactions,^[15] lithium dendrite growth,^[16] and chemo-mechanical failure.^[17] And these

Dr. J. Zhang, C. Zheng, L. Li, Dr. Y. Xia, Prof. H. Huang, Y. Gan, Dr. C. Liang, Dr. X. He, Prof. X. Tao, Prof. W. Zhang
College of Materials Science and Engineering
Zhejiang University of Technology
Hangzhou 310014, P. R. China
E-mail: msechem@zjut.edu.cn

 The ORCID identification number(s) for the author(s) of this article can be found under <https://doi.org/10.1002/aenm.201903311>.

DOI: 10.1002/aenm.201903311

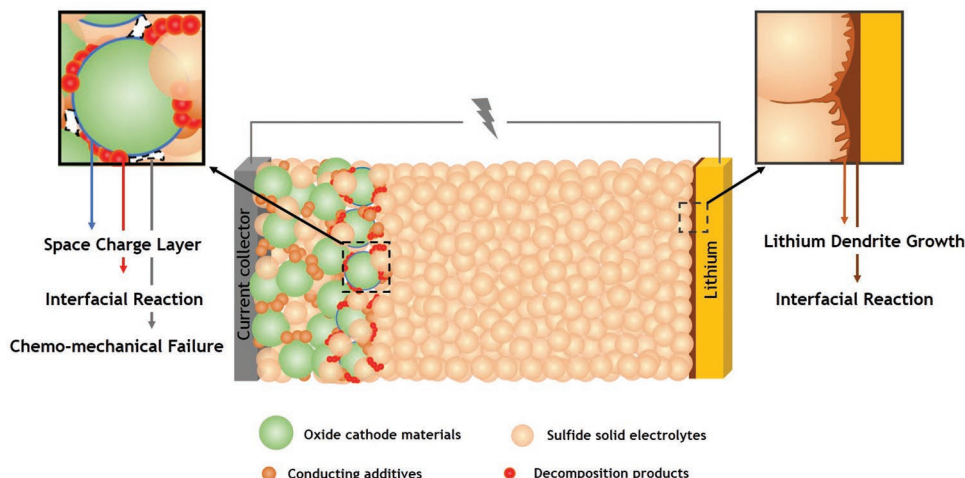


Figure 1. Schematic diagram of five negative factors at interfaces in ASSLBs with oxides as active materials and sulfides as electrolytes.

problems occur mainly at the interfaces between the sulfide-type SEs and two electrodes. These negative interfacial characteristics in ASSLBs with oxides as active materials and sulfides as electrolytes are schematically described in **Figure 1**. To investigate the effects and mechanisms of interfaces, a lot of in situ or ex situ characterization methods have been applied to interface researches over several years.^[15b,d,17b,c,18]

For the sulfide-type electrolytes/cathode interface, when a layered oxide cathode contacts with one of sulfide-type electrolytes, the high electrochemical potential of cathode makes Li^+ easy to transfer from the electrolyte side to the cathode side. For high ionic conductivity sulfide electrolytes, lithium concentration at interface rapidly decreases because of weak molecular interaction, resulting in the lithium-depleted layer.^[14a] This layer at interface is also defined as the SCL, which increases interfacial resistance and interfacial polarization.^[19] And the SCL effect has been verified to be of great importance for ion transport in the nanometer-scale interfaces by some theoretical and experimental researches.^[14,19,20] Tateyama and co-workers elucidated the formation of SCL at $\text{LiCoO}_2/\beta\text{-Li}_3\text{PS}_4$ interface and the effect of LiNbO_3 buffer material by using the density functional theory (DFT) method.^[14b] It has been universally found that SCL can be indirectly demonstrated by interfacial impedance and the small potential slope at the beginning of the first charge curve. The potential slope gradually shortens with increasing thickness of the surface coating layer (such as LiNbO_3 , LiTaO_3 , $\text{Li}_4\text{Ti}_5\text{O}_{12}$, and Li_2SiO_3) but the interfacial resistance changes as an arc decreased, which means that uniform buffer layer with an appropriate thickness can dramatically suppress the formation of SCL.^[20a] The types, thickness, uniformity, and preparation methods of the buffer materials could affect the inhibiting effect to different extent. However, because of theoretical insufficiency (ambiguous Li^+ diffusion mechanism in the buffer layer) and technical defect (inadequate coating technology), the buffer layers may introduce two new interfaces, which can bring many indistinguishable interfacial resistances and make Li^+ diffusion mechanism more complicated. Using spatially resolved electron energy-loss spectroscopy in a transmission electron microscope mode (SR-TEM-EELS) can visualize the Li^+ distribution in nanometer

scale. Furthermore, some in situ characterization methods have been applied to this research field in recent years. In situ electron holography (EH) and in situ scanning probe microscopy (SPM) visually show the Li^+ movement and the potential distribution near the electrode/electrolyte interface in the first cycle, which reveals the details where SCL occurs.^[21]

In addition to SCL, the interfacial reaction is another important factor influencing electrochemical performance of ASSLBs. X-ray photoelectron spectroscopy (XPS) result confirms that sulfates, phosphates, elemental sulfur, lithium polysulfide, and sulfides generate at the interface between $\text{Li}_6\text{PS}_5\text{Cl}$ and oxide cathode such as LiCoO_2 , $\text{LiNi}_{1/3}\text{Co}_{1/3}\text{Mn}_{1/3}\text{O}_2$, and LiMn_2O_4 .^[15d] By using Raman experiments, the structural changes at the $\text{LiCoO}_2/\text{Li}_3\text{PS}_4$ interface are observed during charging, which corresponds to Raman spectral changes.^[22] Nuclear magnetic resonance (NMR) has been used to reveal the Li^+ transport over the Li_2S and $\text{Li}_6\text{PS}_5\text{Cl}$ interface, which indicates the negative effect of interface is the major barrier to achieving high-capacity performance of ASSLBs.^[23] Meanwhile, the interfacial reaction between sulfide-type electrolytes and lithium anode also exists along with the lithium dendrite growth. Although the decomposition products are specific to each of sulfide-type SEs, Li_2S with poor electronic and ionic conductivity is produced at all anode interface for ASSLBs, which could result in an unfavorable solid electrolyte interphase (SEI). For the $\text{Li}_3\text{PS}_4/\text{Li}$ interface, it has been found by in situ Raman spectroscopy measurement that a reversible conversion of PS_4^{3-} to $\text{P}_2\text{S}_6^{4-}$ is associated with the formation of intermediate phases (such as Li_2S , Li_3P , etc.) during the Li^+ deposition and stripping.^[18a] Other products have also been found by many characterization methods. It has been discovered by XPS that metallic lithium could reduce $\text{Li}_6\text{PS}_5\text{X}$ ($\text{X} = \text{Cl}, \text{Br}, \text{I}$) and form Li_3P , Li_2S , and LiX at the $\text{Li}_6\text{PS}_5\text{X}/\text{Li}$ interface.^[24] Similar findings have also been elaborated in the research of two other popular solid electrolytes ($\text{Li}_7\text{P}_3\text{S}_{11}$ and $\text{Li}_{10}\text{GeP}_2\text{S}_{12}$).^[15c] The diffusion of all decomposition products into electrolyte near interface could weaken the electrochemical stability of electrolyte. But unlike the others, the SEI formation of $\text{Li}_6\text{PS}_5\text{Cl}$ is very slow in the initial period several cycles.^[24,25]

Recently, another factor influencing interface stability of ASSLBs has been getting some attention,^[17b,c,26] which is the

chemo-mechanical failure. This failure is a combination result of the effect of interfacial reaction, mutual diffusion of elements, and stress concentration at the contact positions. The mechanical failure provokes a contact loss at the sulfide-type electrolytes/cathode interface, which further deteriorates the interface and battery capacity. Especially, the chemo-mechanical volume changes in all-solid-state Li-S batteries with sulfide electrolytes affect electrochemical performance more severely than layered oxides cathode.^[17b,c]

How to form a favorable interface is the key to achieve low-impedance and high-capacity ASSLBs. To deeply reveal the evolution mechanisms of solid/solid interfaces will provide guidance and support for solving these interface problems. However, for now, the dynamic and in situ observations of interface are still limited. There are few research reports describing the mechanisms how the interacted and synthetic effects of multiple negative factors lead to an unstable interface during the initial cycles and long-term cycles. In this work, we presented an in-depth analysis on the interfacial evolution intra and intercycle of argyrodite-based solid battery, which is made up of nickel-rich layered oxide $\text{LiNi}_{0.8}\text{Co}_{0.1}\text{Mn}_{0.1}\text{O}_2$ (NCM) as cathode and $\text{Li}_6\text{PS}_5\text{Cl}$ as solid electrolyte. Through data fitting, with alternately charge and discharge in two initial cycles, in situ electrochemical impedance spectroscopy (EIS) indirectly evaluated the evolution of SCL in unprecedented detail. Furthermore, in situ Raman spectroscopy measurement, which shows extended sensitivity for sulfide-related structural characteristic, was applied to evaluate NCM/ $\text{Li}_6\text{PS}_5\text{Cl}$ interface change during the first cycle. Both in situ testing for evaluating the evolutions of interface is based on the Li^+ movement at NCM/ $\text{Li}_6\text{PS}_5\text{Cl}$ interface. We found that the most important changes in the impedance and Raman spectra both occur in the voltage platform during the first cycle, which relate to the evolution of SCL and chemical bond state of electrolyte at interface. To better understand the mechanisms for unstable interfaces, the interface changes were also examined by ex situ characterizations including scanning electron microscopy (SEM), energy-dispersive spectra (EDS), and XPS. The $\text{Li}_6\text{PS}_5\text{Cl}/\text{Li}$ interface stability was also investigated by these testing methods. We demonstrated some important details about the evolution of interface and disperse a new sight of the operando structural and ionic state changes of sulfide electrolytes.

2. Result and Discussion

2.1. In Situ Impedance Spectroscopy of NCM/ $\text{Li}_6\text{PS}_5\text{Cl}/\text{Li}$ Cell

Interfacial resistance is a comprehensive physical quantity that represents the interface stability, especially SCL. The existence of SCL in ASSLBs with oxide cathodes and sulfide electrolytes is evidenced by a small potential slope at the beginning of the first charge curve.^[14a,20,21] This slope prior to the charging plateau is associated to the applied voltage-induced Li^+ transfer, which changes the charge distribution of SCL. It has also been universally found that SCL can be indirectly characterized by interfacial impedance.^[20a,27] In order to investigate how SCL evolves during the charge/discharge cycles, EIS measurements were conducted every equidistant capacity of 1 or 2 mA h g⁻¹

(corresponding charge/discharge profiles are shown in Figure S1, Supporting Information). **Figure 2** shows the evolution of EIS spectra for the first two cycles at 0.2C with an equidistant capacity of 2 mA h g⁻¹. EIS spectra are presented in the form of Nyquist plots (left column) and Bode plots (right column), respectively. As seen in Figure 2, the change of EIS spectra along with charge-discharge processes is mainly in the low-frequency region, rather than in the high-frequency region. During the beginning of the first charging, the slope gets small in low-frequency region of Nyquist plot and the corresponding curve amplitude change of Bode plot increases with charging potential increasing. The low-frequency curve of Nyquist plot is getting closer to the shape of semicircle. When the initial charge percentage reaches 19.96%, as the open-circuit voltage (OCV) grows to 3.706 V, a regular semicircle occurs in low-frequency region. With the continuous increase of charge potential (OCV > 3.706 V), the impedance curve (including Nyquist plot and Bode plot) has not apparent variation, indicating the charge plateau is a change point of the resistance of ASSLBs. During the first discharge, the impedance curve changes in an opposite trend: after the discharge percentage reaches 68.71% (OCV = 3.671 V), the low-frequency semicircle starts to change and restores previous state. Similar to impedance spectra of the first cycle above, it can also be found a reversible change during the second cycle. The curve seems to be returning to its original state (uncycled NCM/ $\text{Li}_6\text{PS}_5\text{Cl}/\text{Li}$ cell, in Figure 2b, the dotted line) at the latter period of discharge, but quite remarkably, there is not exactly the same as the uncycled state. And compare the impedance at the second discharge ending (99.88%) and after the second discharge, as shown in Figure S2 (Supporting Information), it shows a significant difference. That means there are two different equivalent circuits corresponding to two states of battery (the effect of with or without applied electric field).

Then, we quantified the impedance of NCM/ $\text{Li}_6\text{PS}_5\text{Cl}/\text{Li}$ cell to evaluate the evolution of interfacial impedance shown in **Figure 3** and Table S1 (Supporting Information). All Nyquist plots were fitted into two different equivalent circuits (inset in Figure 3a, "FIT#1" and "FIT#2"). As shown in Figure 3a,b, the model "FIT#2" is required for a sufficient fit of the impedance spectrum of uncycled battery state, the model "FIT#1" for other states. The only difference between these two equivalent circuits is their modeled element corresponding the low-frequency region. In contrast to the Warburg diffusion element W (in "FIT#2"), there is an unusual Nernst diffusion element N (in "FIT#1") which is limited to low frequency due to a finite-length restricted diffusion.^[28] The Nernst diffusion is controlled by the Warburg coefficient W ($\Omega \text{ s}^{-1/2}$) and the Nernst constant k_N (s^{-1}) in Equation (1)

$$Z_N = \frac{W}{\sqrt{j \cdot \omega}} \tan h \sqrt{\frac{j \cdot \omega}{k_N}} \quad (1)$$

For the finite diffusion (N), it usually shows an additional semicircle in the low-frequency region of Nyquist plot, a straight line for the infinite diffusion (W). So these two equivalent circuits could effectively fit the impedance spectra in this work. Two different equivalent circuits are constructed to

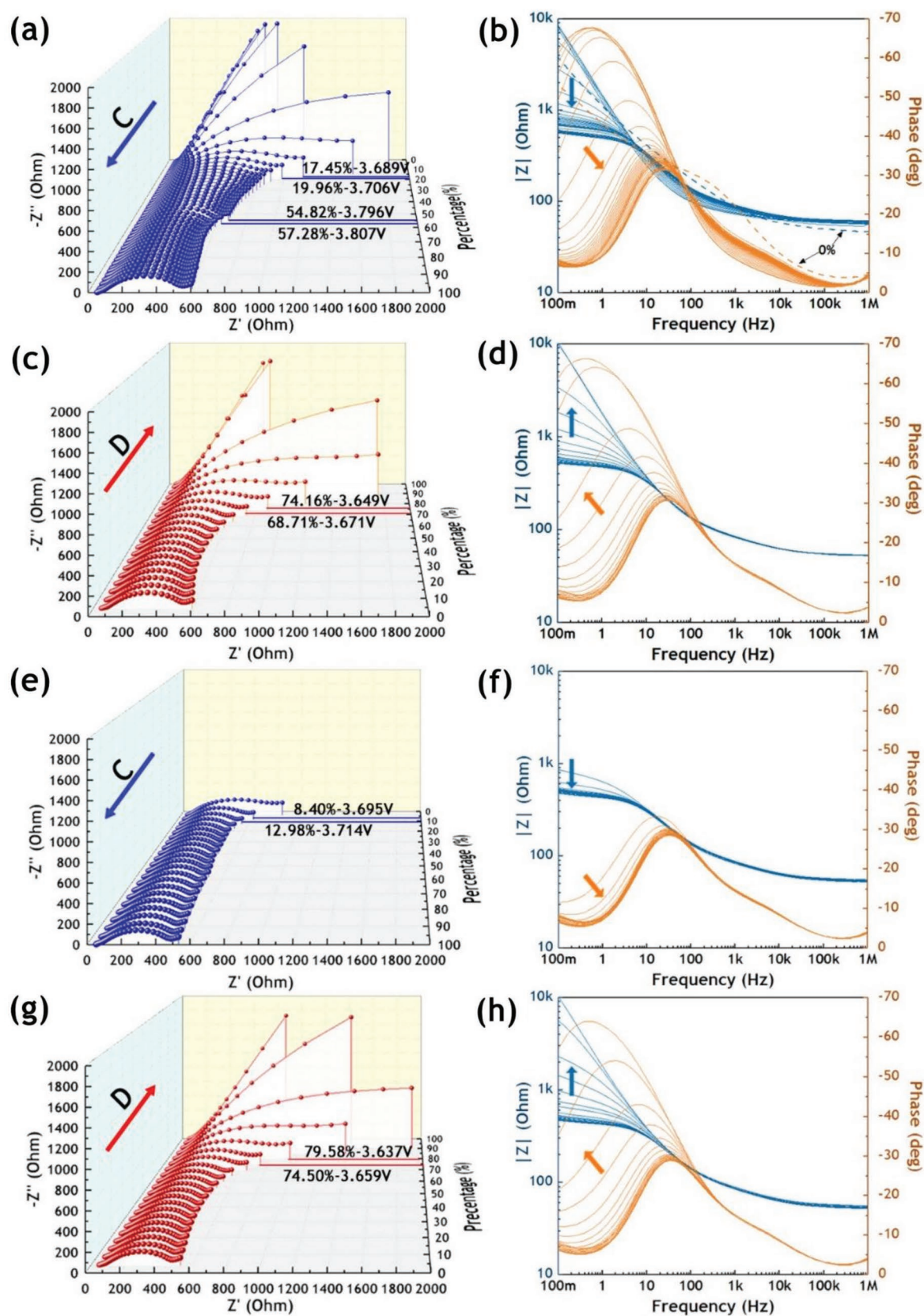


Figure 2. In situ impedance spectra of NCM/Li₆PS₄/Li cell at 0.2C with equidistant capacity of 2 mA h g⁻¹ during the first two cycles. a,c,e,g) Nyquist plots and b,d,f,h) Bode plots of the impedance spectra during the charge ("C") and discharge ("D") processes.

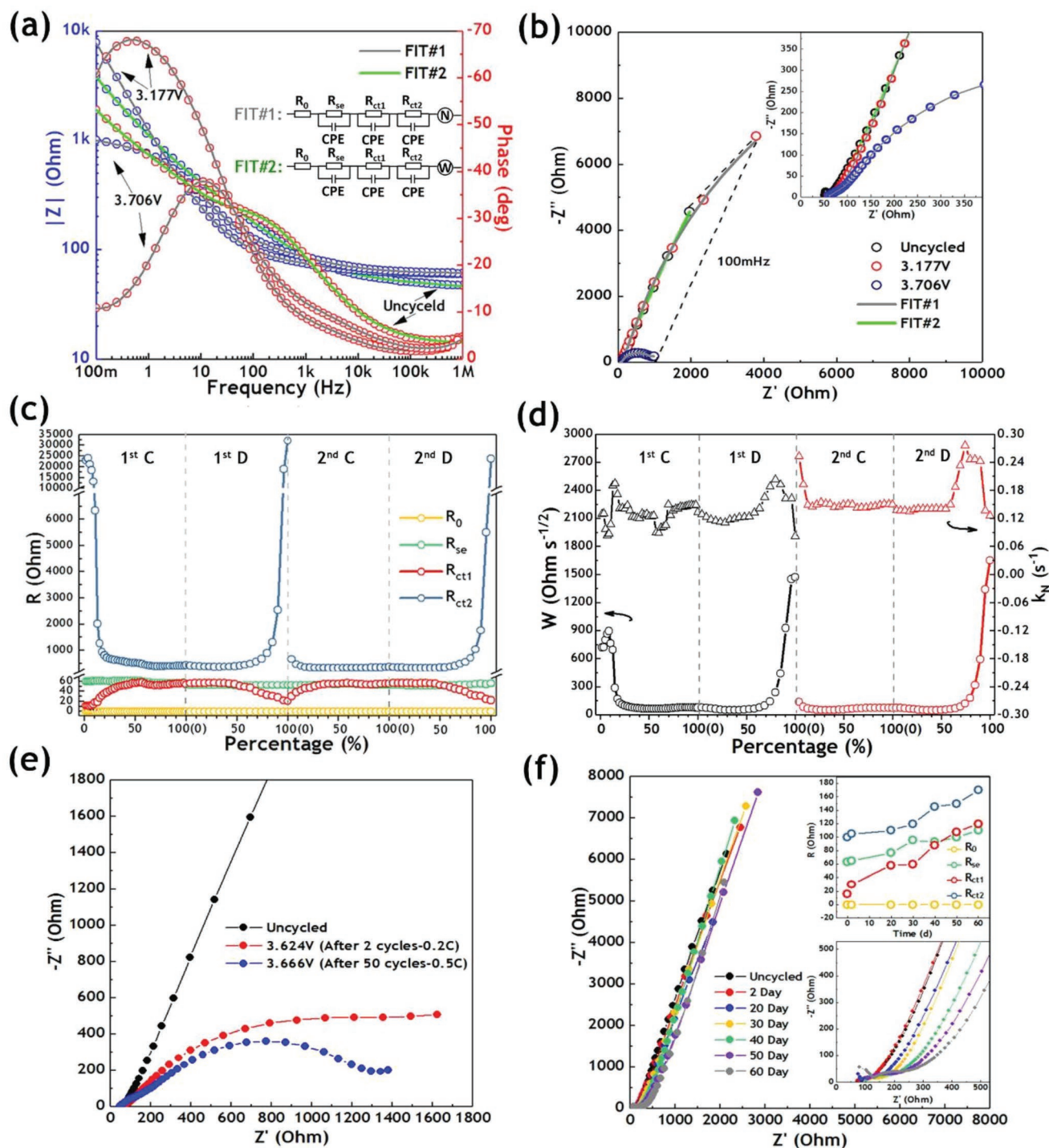


Figure 3. a,b) Examples of Bode plot and Nyquist plot obtained by fitting the in situ impedance spectra at three voltages (before cycling, 3.177 V and 3.706 V in the first charge). The circles represent the experimental data, the lines represent the fitted data based on two equivalent circuits (inset in Nyquist plot, “FIT#1” and “FIT#2”). c) Variation of the resistance values, and d) the Warburg coefficient W and the Nernst constant k_N with the charge–discharge processes obtained by fitting the impedance spectra. e) Nyquist plot of NCM/Li₆PS₅Cl/Li cell: before cycling (“uncycled”), after two cycles at 0.2C (in situ EIS measurement at 0.2C), after 50 cycles at 0.5C (carried out after in situ EIS measurement). f) Evolution of Nyquist plot and resistance values for fresh battery during various storage days.

distinguish common resistances: R_0 , R_{se} , R_{ct1} , and R_{ct2} , representing the current collector resistance, bulk resistance, and two interfacial resistances. The R_{ct1} and R_{ct2} values show a reversible

change during the first two cycle, but not the R_0 (≈ 2 m Ω) and R_{se} (≈ 60 Ω). Compared by the R_{ct1} and the R_{ct2} values, there is a highly variable trend of the R_{ct2} and a large difference value

($\approx 540 \Omega$) between the two even if the values fluctuate slightly. We speculate the R_{ct1} and R_{ct2} represent the interfacial resistance between lithium and electrolyte, interfacial resistance between cathode and electrolyte, respectively.

To further confirm the attribution of R_{ct1} and R_{ct2} , a Cu/Li₆PS₅Cl/Li cell and a NCM/Li₆PS₅Cl/In cell were assembled. The Cu/Li₆PS₅Cl/Li cell was used to investigate the impedance change of Li plating and stripping at the interfaces. As shown in Figure S3 (Supporting Information), whether in the cyclic voltammetry (CV) cycles or in the battery cycles with constant capacity (converted from specific capacity at 0.2C), the resistance values did not vary by larger orders of magnitude. We also assembled all-solid-state cell with indium instead of lithium as anode, since indium is considered as a nonreactive anode with sulfide-type SEs.^[29] The impedance change of the NCM/Li₆PS₅Cl/In cell after two cycles at the same current density (at 0.2C) are presented in Figure S3f (Supporting Information), which shows very similar profile with the NCM/Li₆PS₅Cl/Li cell. This evidence reinforces our speculation about the R_{ct1} and R_{ct2} attribution.

As seen from Figure 3c and Table S1 (Supporting Information), the R_{ct1} and R_{ct2} values have a reversible change during the first two cycles. However, the R_{ct2} value in one cycle varies sharply, confirming that the applied electric field could cause a great change of interfacial resistance in the NCM/Li₆PS₅Cl/Li cell. The electrode kinetics of battery can be reflected by the Faradaic impedance, consisting of the charge-transfer resistance

(R_{ct}) and the Nernst impedance (Z_N).^[30] As shown in Figure 3d, we investigated the variation of the Warburg coefficient W and Nernst constant k_N , which reflect the mass-transport process (Li⁺ diffusion process) in electrode.^[28a,30a,31] Similarly, there are reversible tendency and saltation point during cycling. Besides, the impedance evolution of fresh battery at different time was monitored shown in Figure 3f. There is no larger impedance change and no additional semicircle in low-frequency region, which could exclude the effect of internal instability. We also investigated the in situ EIS measurement at 0.5C (Figures S4 and S5 and Table S2, Supporting Information). Along with increasing charge–discharge rate, the interfacial resistance generally increases but the impedance change shows a similar rule.

2.2. Ex Situ Characterizations of NCM/Li₆PS₅Cl/Li Interfaces

For above-mentioned tremendous R_{ct2} change at the early stage of cycling, ex situ characterizations (XPS, SEM, and EDS) were performed to verify if interfacial reaction is the cause of this change. Figure 4 shows the S 2p and Li 1s spectra of NCM/Li₆PS₅Cl interface and Li₆PS₅Cl/Li interface at various states after charge/discharge processes at 0.5C. Before cycling, the S 2p spectra can be deconvoluted into three components:^[15d,18b,24,25] a major doublet with the S 2p_{3/2} at the binding energy of 161.7 eV (red) can be associated with the S atoms (in P–S–Li) of argyrodite, a small amount of component with the S 2p_{3/2} at

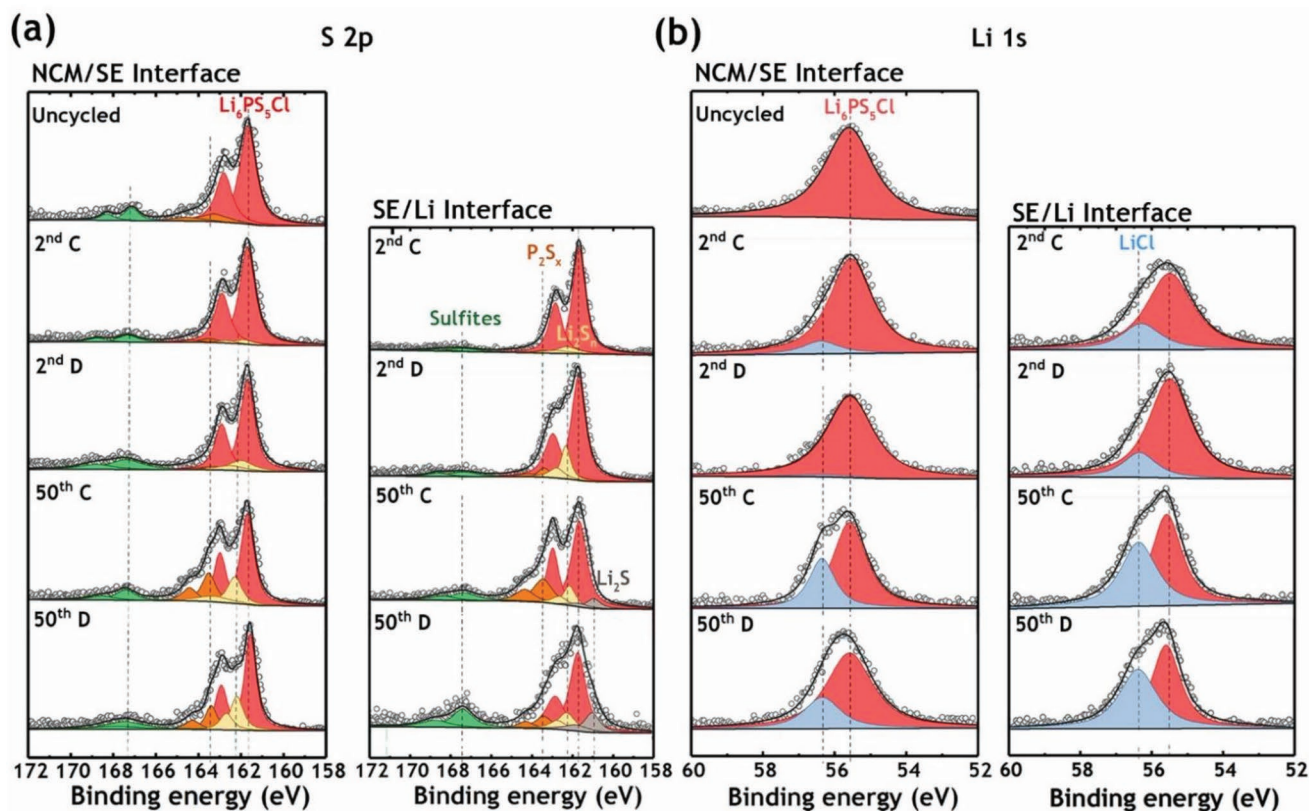


Figure 4. a,b) S 2p and Li 1s XPS spectra at two interfaces (NCM/Li₆PS₅Cl interface and Li₆PS₅Cl/Li interface) of NCM/Li₆PS₅Cl/Li cell: before cycling ("uncycled"), after the second charge ("2nd C"), and discharge ("2nd D"), after the 50th charge ("50th C") and discharge ("50th D") at 0.5C.

163.5 eV (orange) can be assigned to polysulfide (P_2S_x), and an additional component at 167.1 eV (green) can be explained by trace of the sulfite (SO_3^{2-}) (because of the reagent used for the synthesis). With regard to Li 1s spectra, the signal of lithium at 55.6 eV mainly comes from argyrodite for characterizations at NCM/ Li_6PS_5Cl interface and another signal comes from lithium metal at Li_6PS_5Cl/Li interface. After two cycles, a new component appears with the S $2p_{3/2}$ at 162.1 eV (yellow) in the S 2p spectra and another new component appears at 56.4 eV (blue) in the Li 1s spectra at both interfaces, associated with lithium polysulfide (Li_2S_n) and LiCl, respectively. For the NCM/ Li_6PS_5Cl interface, the XPS spectra have no obvious change whether after charging or discharging, except for the appearance of a negligible amount of Li_2S_n and LiCl. This observation suggests that significant interfacial reaction will not occur in cathode interface during the initial period several cycles. After 50 cycles, the amounts of P_2S_x , Li_2S_n , and LiCl are significantly increased at both interfaces and a last additional component at 160.9 eV (gray) shows up at Li_6PS_5Cl/Li interface, attributed to lithium sulfide (Li_2S), suggesting that the interfacial reaction occurs appreciably because of the decomposition of argyrodite and the growth of lithium dendrite.^[24,32] Therefore, this

confirms that the interfacial reactions become severer at both interfaces and interfacial products accumulate with cycling.

As seen from the morphologies and elemental distribution at NCM/ Li_6PS_5Cl interface in Figure 5a and Figure S6 (Supporting Information), the active material NCM particles are well embedded in the solid electrolyte and there is no decomposition happened before cycling, which results in a dense composite and a low interfacial resistance. After two cycles, the NCM particles refine to many secondary particles but the ball-shaped structure still maintain. The volume change of NCM during lithium deintercalation and intercalation is probably the main reason for this phenomenon.^[17b] After 50 cycles, the NCM particles decompose seriously and the secondary particles scatter on the interface area. Besides, the elemental mappings also show that S, P, and Cl have an in-diffused tendency. The morphologies (surface and cross-section) and corresponding elemental distribution of the interface in contact with lithium are presented in Figure 5b. As mentioned in our previous work, the growth of lithium dendrite and Cl segregation (LiCl demonstrated in the XPS spectra) are remarkable after 50 cycles. We also investigated the morphologies at the interface between cathode and Al current collector. As shown in Figure S7

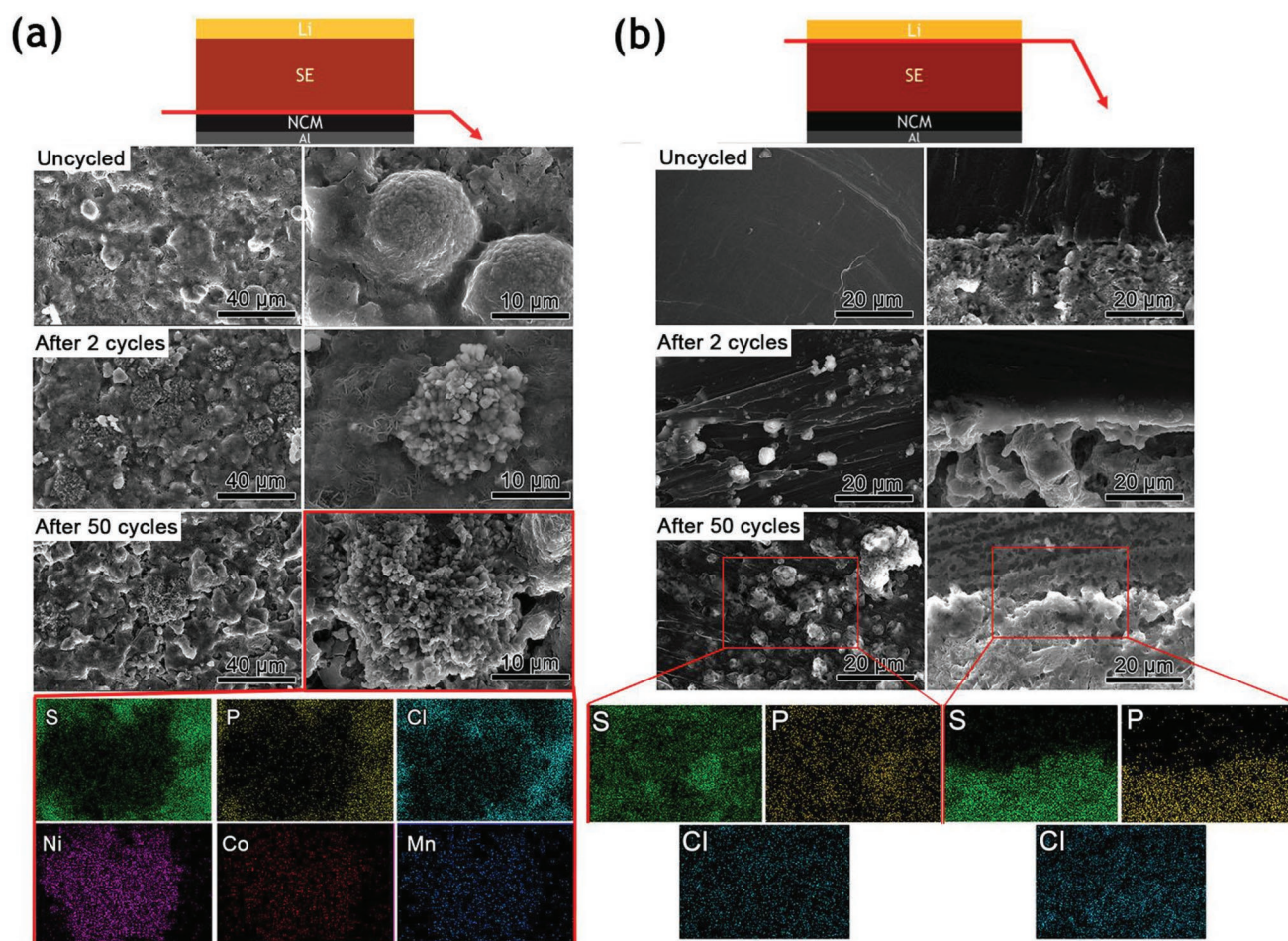


Figure 5. a,b) The SEM images at NCM/ Li_6PS_5Cl interface and at Li_6PS_5Cl/Li interface before cycling ("uncycled"), after 2 cycles and after 50 cycles at 0.5C. The cross-section morphologies of Li_6PS_5Cl/Li interface are on the far right. The elemental mappings at the bottom corresponding to the SEM images (after 50 cycles) in red boxes.

(Supporting Information), after 50 cycles, the big gaps and cracks occur between the NCM particles and the solid electrolyte due to stress concentration, also known as chemo-mechanical failure.^[17b,c]

2.3. In Situ Raman Spectroscopy of NCM/Li₆PS₅Cl/Li Cell

In order to further investigate the evolution of NCM/Li₆PS₅Cl interface in the charge process, we conducted in situ Raman spectroscopy measurement at the interface during CV cycling in a home-made spectro-electrochemical cell (Figure S8, Supporting Information). Based on the change of Raman peak intensity near the NCM particle in optical microscopy image (Figure S9a, Supporting Information), we chose the “point#4” as

the in situ monitor point. As shown in Figure 6a, the in situ Raman spectra in low wavenumber region were obtained as potential series with a sweep rate of 0.5 mV s⁻¹ (sequentially recorded spectra for 0.1 V interval in Figure S9b, Supporting Information). During CV cycling, the Raman peaks have a fluctuant change at 418 and 425 cm⁻¹, the latter is associated with the stretching vibration of PS₄³⁻ (ortho-thiophosphate) from the ionic formula (Li⁺)₆(PS₄³⁻)S₂²⁻Cl⁻.^[12,33] For the other peak at 418 cm⁻¹, it also appeared in the same region in other works, which originated from different PS₄³⁻ vibrational modes due to the presence of other anion.^[5a,34] So it is well-documented to conclude that the peak is associated to another vibration mode of P–S bond in PS₄³⁻. Unlike many reports on sulfide-type electrolytes,^[18a,34,35] there is no obvious molecular conversion of PS₄³⁻ to P₂S₆⁴⁻ (at 410 cm⁻¹) and P₂S₇⁴⁻ (at 390 cm⁻¹), suggesting the

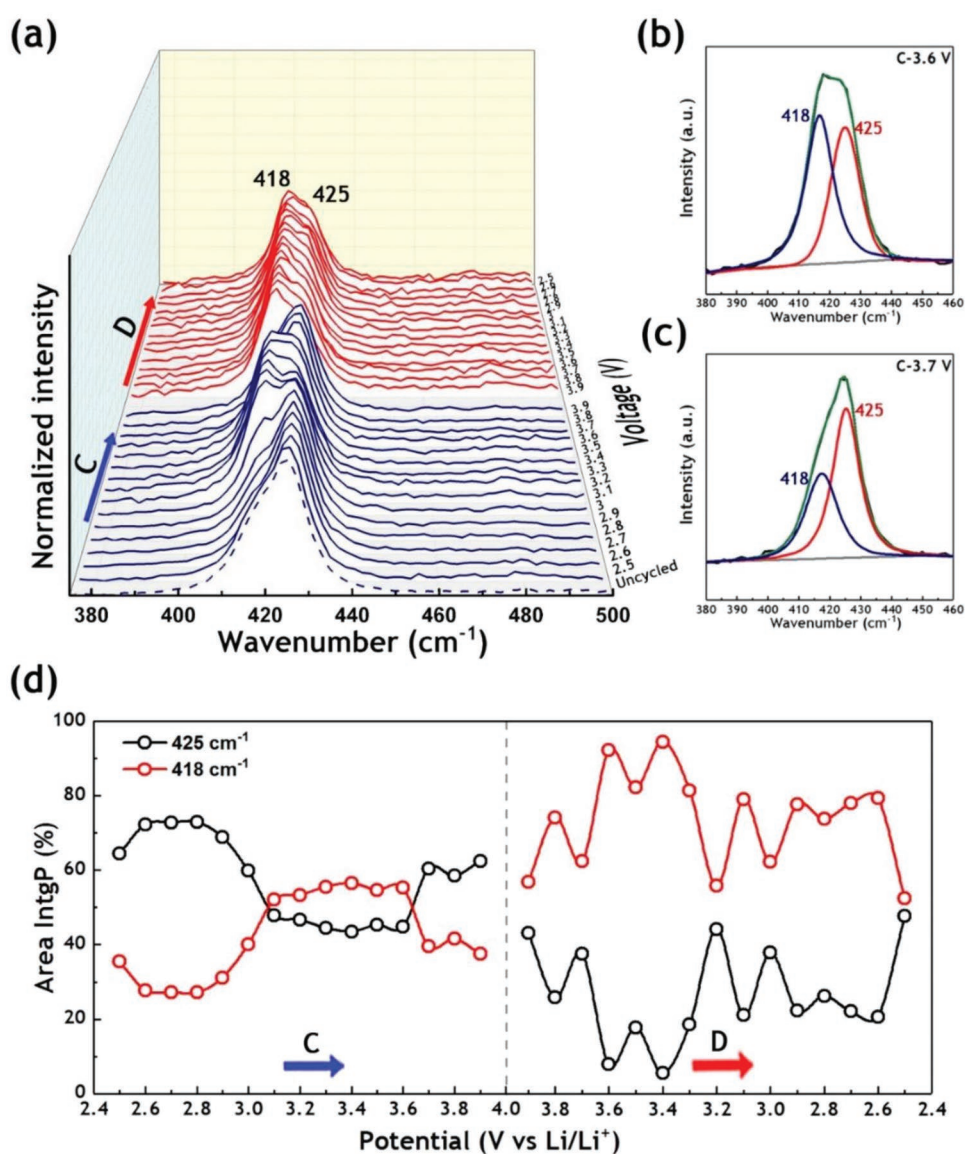


Figure 6. a) In situ Raman spectra at NCM/Li₆PS₅Cl interface during the positive and negative potential sweeps. b, c) Examples of normalized peak fitting results from in situ Raman spectra at NCM/Li₆PS₅Cl interface at two voltages (3.6 and 3.7 V in the first positive potential sweep). d) Normalized peak area percentages evolutions of two Raman peaks at 418 and 425 cm⁻¹ during the positive and negative potential sweeps.

composition and structure of $\text{Li}_6\text{PS}_5\text{Cl}$ at the interface remain intact during the first cycling. We normalized the intensities of all the Raman spectra and fitted curves in low wavenumber region (such as Figure 6b,c). The normalized peak area percentages calculated from the two peaks (at 418 and 425 cm^{-1}) are shown in Figure 6d, along with the potential-dependent change. When the positive sweep starts from 2.5 to 3.6 V, the intensity of the peak at 418 cm^{-1} increases and this peak gradually becomes a dominant role, which indicates gradual enhancement of corresponding vibration of PS_4^{3-} . At the 3.7 V charge plateau, the intensities of both peaks quickly recover to original level and the peak at 425 cm^{-1} takes hold again. During the negative sweep, the peak at 418 cm^{-1} has always played a dominant role but the area percentages or intensities of both peaks completely differ from the ones during the positive sweep. On the basis of the above-mentioned change between two peaks, we can conclude there are three stages of the vibration change in PS_4^{3-} at the interface. Among many researches on structural changes at the interface for sulfide-type electrolytes, it is found that the reversible structural (the association and dissociation of the S–S bonds between the PS_4^{3-} units) and electronic state changes of Li_3PS_4 occurred during the charge–discharge processes.^[34] But in our work, as the Raman and XPS spectra have shown, it is a different situation that the structural change of $\text{Li}_6\text{PS}_5\text{Cl}$ at the interface is only limited to the vibration of PS_4^{3-} in the early stage of cycling, because of the presence of S^{2-} and PS_4^{3-} in cubic crystal structure. After a long-term cycling,

the PS_4^{3-} units (Figure S9d, Supporting Information) appeared in the interior of NCM particles, which further confirms the NCM particles decompose seriously and the S, P elements diffuse to the interior, as mentioned in XPS and SEM sections.

2.4. Evolution of NCM/ $\text{Li}_6\text{PS}_5\text{Cl}$ Interface during the Early Cycles

All available evidence indicates that, due to the effect of applied electric field, the $R_{\text{ct}2}$ change is mainly caused by the Li^+ redistribution at interface. In other words, the formation of SCL may be origin. It is apparently that, when the uncycled cells start to charge, the $R_{\text{ct}2}$ value varies sharply. The similar sort of phenomenon crops up in the moment when the first discharge ending turns into the second charge starting, even for a while after the second discharge. That means the effect of applied electric field could cause the huge changes of SCL, which results in the changes of interfacial resistance at different stages of cycling. Based on many theoretical and experimental research about the SCL, the diffusion barrier of SCL can enlarge the interfacial resistance and the polarization.^[14,19] Therefore, how the Li^+ transfer and concentration distribution in SCL is important to understand the discontinuous changes of impedance.^[27] Based on the impedance spectra, we describe the Li^+ migration and concentration distribution under equilibrium states (uncycled and after cycling) and charge–discharge states, as shown in Figure 7. When the uncycled state turns into the charging state,

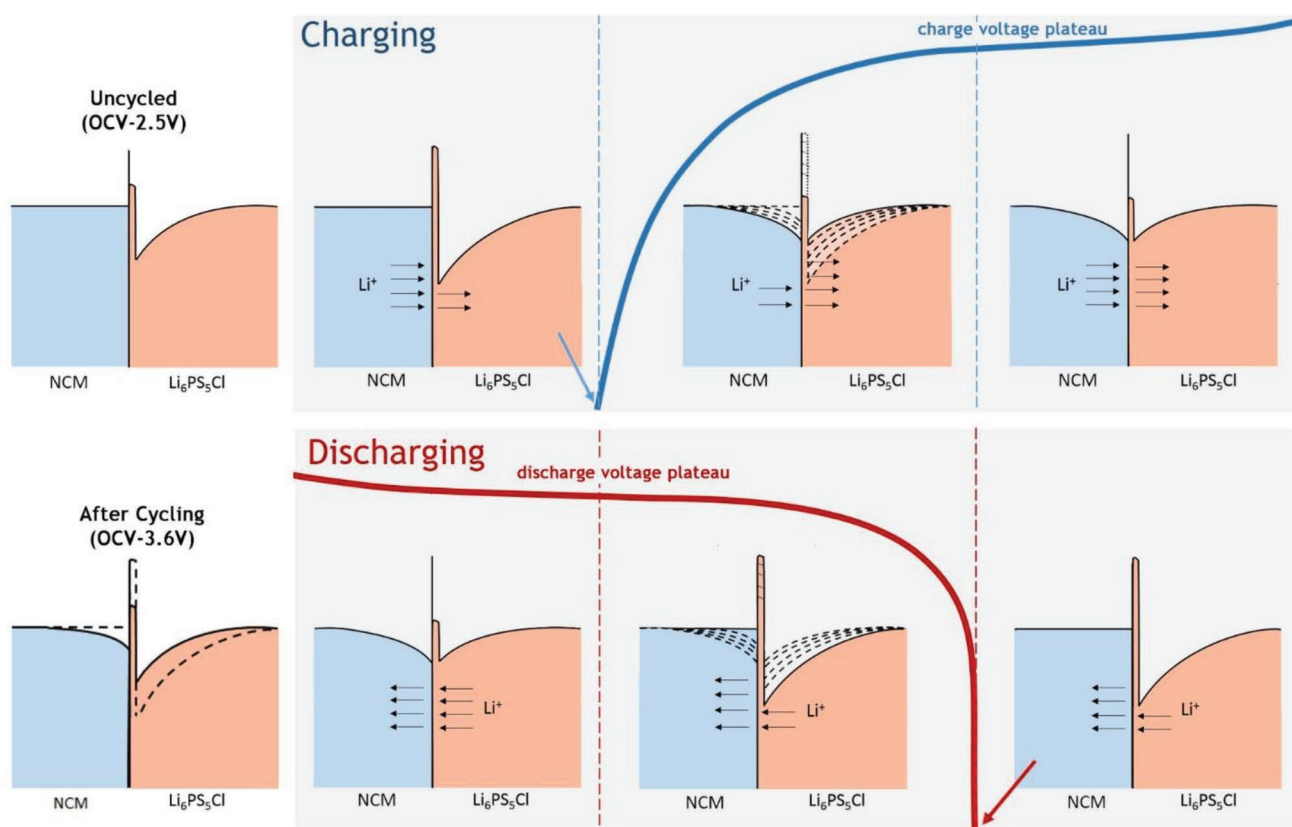


Figure 7. Schematic illustrations of the Li^+ concentration and Li^+ migration at NCM/ $\text{Li}_6\text{PS}_5\text{Cl}$ interface: before cycling (“uncycled”), during the first charge–discharge process, and after cycling.

Li^+ starts to deintercalate from layered NCM and migrate from the cathode side to the lithium anode side. But in this moment, the amount of Li^+ migration from the $\text{Li}_6\text{PS}_5\text{Cl}$ side is much less than the deintercalation from NCM, because of the diffusion barrier of SCL. That can make the accumulation of a great amount of lithium ions near the NCM side, which results in the rapid increase of R_{ct2} value. As the battery is charging, the Li^+ concentration near the $\text{Li}_6\text{PS}_5\text{Cl}$ side will gradually increase with the accumulated Li^+ migrating to the $\text{Li}_6\text{PS}_5\text{Cl}$ side to replenish the Li interstitial sites in lithium-depleted layer (known as SCL). And Li^+ concentration near the NCM side has a reverse trend because of continuous deintercalation. After the electrochemical potential near the $\text{Li}_6\text{PS}_5\text{Cl}$ side reaches about the charge plateau, the concentrations of both side are stable and Li^+ migration reaches a dynamic balance, which indicate the SCL tends to be stable. Correspondingly, the R_{ct2} value gradually descends and tends to be constant, so does the slope in the voltage profile. For the discharging process, as Li^+ migrates in the opposite direction, the Li^+ concentration distribution has an opposite trend like the above-mentioned impedance change. There are no obvious changes in the concentration distribution and SCL until the discharge potential reaches the discharge plateau. At the end of the first discharge, Li^+ starts to accumulate near the NCM side because Li^+ intercalates fully into NCM and the Li^+ concentration decreases gradually near the $\text{Li}_6\text{PS}_5\text{Cl}$ side because the

oxide has an attraction to Li^+ . However, R_{ct2} value varies sharply from the first discharge ending to the next charge starting, even after the second discharge. Meanwhile, the starting OCV becomes at ≈ 3.6 V, with a flatter charging curve comparing with the first cycle. This can be explained by that Li^+ migrates instantaneously to the $\text{Li}_6\text{PS}_5\text{Cl}$ side to reach an equilibrium state due to the disappearance of the applied electric field. Apparently there is a trend to go back to the original SCL state. But considering the difference of battery impedance and interface structure before and after cycling, as demonstrated by ex situ characterizations, the SCL may not return perfectly. So we can deduce that the SCL redistribution has finished after the first cycle and the SCL change is rapid and relatively reversible in the following cycles.

With the combined analysis of the potential-dependent changes in the in situ Raman spectra and in situ impedance spectra, there are some transitions happen at the same potentials (especially at the charge plateau) in two testing results. So one can estimate that the Li^+ migration can also cause the different vibration in PS_4^{3-} at NCM/ $\text{Li}_6\text{PS}_5\text{Cl}$ interface, except for the change of SCL. **Figure 8** illustrates the NCM/ $\text{Li}_6\text{PS}_5\text{Cl}$ interface evolutions during the charge–discharge processes based on the SCL and different vibration states of P–S bond in PS_4^{3-} . Before cycling, there is no Li^+ migration at NCM/ $\text{Li}_6\text{PS}_5\text{Cl}$ interface. As described in the SCL section, under an applied electric field, Li^+ will migrate from NCM to the SCL (near the $\text{Li}_6\text{PS}_5\text{Cl}$ side) to

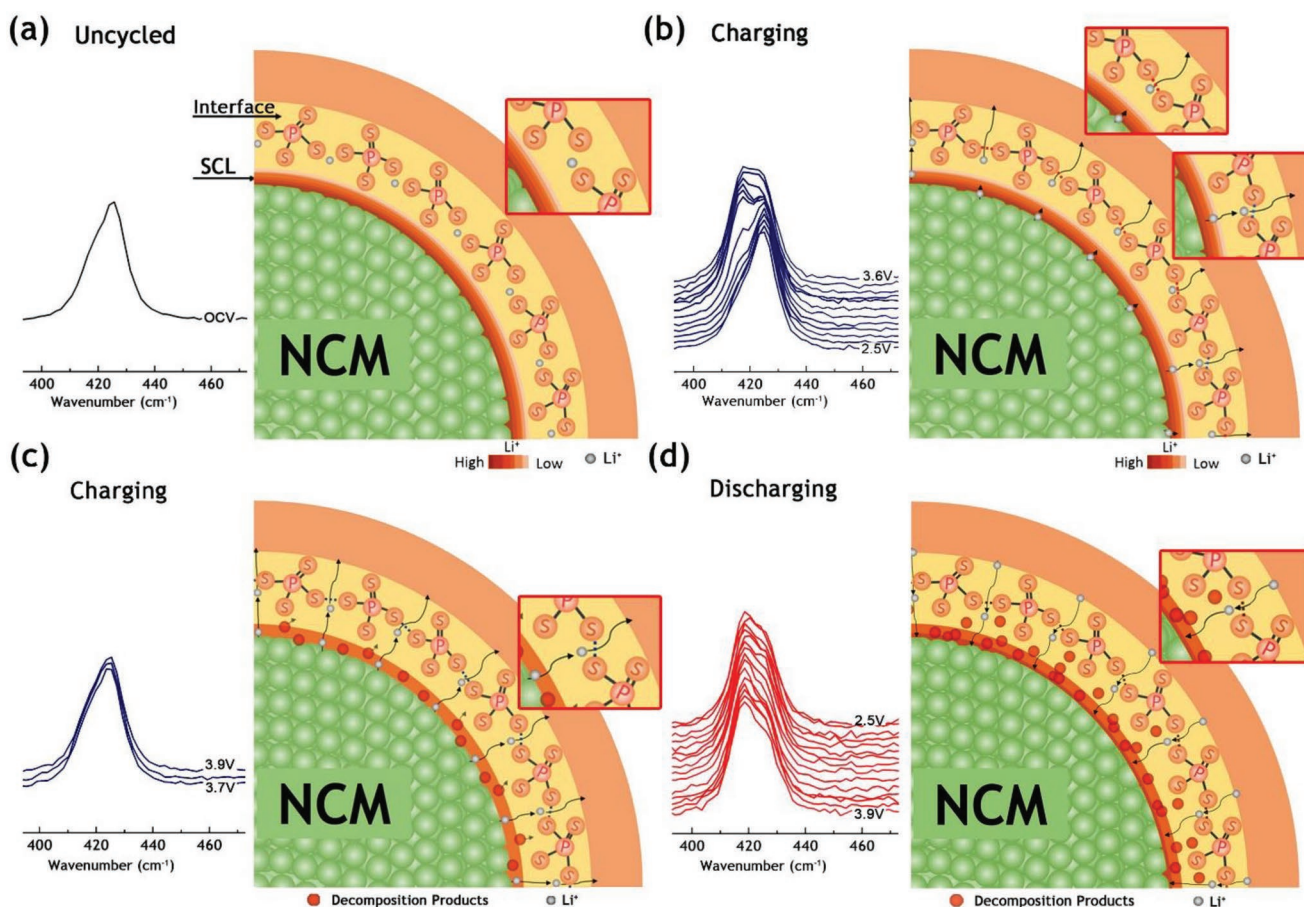


Figure 8. a–d) Schematic illustrations of interfacial evolution during the charge–discharge processes based on different vibration states of P–S bond in PS_4^{3-} at NCM/ $\text{Li}_6\text{PS}_5\text{Cl}$ interface.

replenish the Li interstitial sites, and Li^+ in electrolyte at interface will migrate into the inside, so there are two kinds of Li^+ migration paths at interface (two enlarged portions in Figure 8b). These two paths can change the mutual attraction between the PS_4^{3-} , thereby causing two kinds of P–S bond. With increasing potential, the Li^+ concentration will gradually increase near the $\text{Li}_6\text{PS}_5\text{Cl}$ side in lithium-depleted layer (SCL), which causes the intensity of the peak at 418 cm^{-1} increases and gradually becomes a dominant role. After the potential reaches about 3.7 V charge plateau, the SCL is stable and no longer affects the Li^+ migration (in Figure 8c), that is, all the Li^+ successively migrate from the NCM to the interface to the internal electrolyte, accompanied by the interfacial decomposition reaction. The Raman spectra show a similar vibration state of the PS_4^{3-} because the ion migration is a persistent equilibrium. And the discontinuous vibration state change of the PS_4^{3-} occurs between 3.6 and 3.7 V, corresponding to the large change of impedance during the first charge process in the same potential range. During the discharge process, as the Li^+ migrates from the internal electrolyte back to the NCM, the opposite direction of migration cause another vibration state of the PS_4^{3-} , then the change of SCL at the discharge ending and the diffusion of decomposition products also bring a slight fluctuation of two Raman peaks (Figure 8d).

3. Conclusions

Interfacial property is one of the most important issues of all-solid-state batteries. In this paper, we provide an in-depth understanding of the interface evolution at NCM/ $\text{Li}_6\text{PS}_5\text{Cl}$ interface by using in situ and ex situ characterizations. Through comparative analysis of all the factors, we found that the SCL played a leading role to the interfacial impedance change at the early stage of cycling. The interfacial evolution was mainly due to the Li^+ migration states change with the effect of applied electric field. Simultaneously, the Li^+ migration can also cause a slight change of PS_4^{3-} structure at interface. With the increasing times of cycling, because of the multiple impacts including the SCL, interfacial reactions, chemo-mechanical failure, and lithium dendrite, the interfaces gradually deteriorated and the corresponding interfacial resistances obviously increased, whether at the cathode side or the anode side. Therefore, the long-term battery degradation mechanisms become complicated, and further investigation about detailed mechanism is necessary in the future. These findings enlighten us that establishing an effective buffer mechanism between highly conductive oxide and sulfide may be a key for the design and optimization of ASSLBs.

4. Experimental Section

Fabrication of All-Solid-State Battery: The solid electrolyte $\text{Li}_6\text{PS}_5\text{Cl}$ and the composite cathode were prepared using method by described in a previous work.^[11] In brief, stoichiometric mixture of laboratory-grade Li_2S , P_2S_5 (99%, Aladdin) and LiCl (99.99%, Aladdin) was milled at 500 rpm for 24 h. Subsequently, the mixture was sealed in a stainless steel tube and annealed at 500°C for 2 h to obtain argyrodite $\text{Li}_6\text{PS}_5\text{Cl}$. The composite cathodes (commercial $\text{LiNi}_{0.8}\text{Co}_{0.1}\text{Mn}_{0.1}\text{O}_2$: $\text{Li}_6\text{PS}_5\text{Cl}$:carbon black:ethyl cellulose (Aldrich) were dispersed with anhydrous ethanol (<0.003% H_2O , Sigma-Aldrich) in mass ratio (of 75:15:9:1) under continuous stirring for

6 h. Then the slurry was coated onto carbon-coated aluminum foil and dried at 80°C for 24 h. For the assembly of NCM/ $\text{Li}_6\text{PS}_5\text{Cl}$ /Li cells, the positive electrode was covered with 80 mg electrolyte powder and pressed together under 350 MPa in a stainless steel tank with a diameter of 12 mm. After that, lithium as the counter electrode was attached on the other side of SE layer and the thickness of ASSLBs was about 600 μm . At last, three-layered pellet was assembled with a 2025 coin-type cell. For the NCM/ $\text{Li}_6\text{PS}_5\text{Cl}$ /In cell, an indium foil as the anode was attached on the other side of SE layer, and the assembling procedure remained exactly the same. For the Cu/ $\text{Li}_6\text{PS}_5\text{Cl}$ /Li cell, a Cu foil is used as working electrode instead of NCM with the same assembling procedure. All the procedures were carried out in an Ar-filled glove box (H_2O and O_2 < 0.5 ppm).

Electrochemical Test: Galvanostatic discharge–charge tests of NCM/ $\text{Li}_6\text{PS}_5\text{Cl}$ /Li cells were performed in a potential range from 2.5 to 4.0 V (vs Li^+/Li) at various current densities (based on $1\text{C} = 200\text{ mA g}^{-1}$) using a Neware battery test system (Neware, Shenzhen). NCM/ $\text{Li}_6\text{PS}_5\text{Cl}$ /In cells were tested in a potential range from 1.9 to 3.4 V (vs In), corresponding to 2.5 to 4.0 V (vs Li^+/Li). CV measurements were conducted on a CHI660D electrochemical workstation (Chenhua, Shanghai). The CV curves of NCM/ $\text{Li}_6\text{PS}_5\text{Cl}$ /Li cell were recorded in the potential range from 2.5 to 4.0 V with a sweep rate of 0.5 mV s^{-1} . The CV curves of Cu/ $\text{Li}_6\text{PS}_5\text{Cl}$ /Li cell were recorded in the potential range from -0.1 to 1.5 V with a same sweep rate. For further tests of plated and stripped Li, Li was plated followed by charging the Cu/ $\text{Li}_6\text{PS}_5\text{Cl}$ /Li cell to 1.0 V to strip the deposited Li (at $35.3\text{ }\mu\text{A cm}^{-2}$) for 1 h by the Neware tester. EIS was obtained using Zennium electrochemical workstation (ZAHNER, Germany), in which the frequency range from 100 mHz to 1 MHz with an amplitude of 10 mV.

In Situ Impedance Spectroscopy: The in situ impedance spectroscopy was measured using a script application of the Zennium electrochemical workstation, which allows automated direct current (DC) cycling with EIS during ramps and rest phases for analyzing ageing effects on the characteristics of the battery. NCM/ $\text{Li}_6\text{PS}_5\text{Cl}$ /Li cells were cycled at 0.2 and 0.5C, which recorded EIS on the charge–discharge phases with equidistant capacity of 2 and 1 mA h g^{-1} , respectively. The frequency range was 100 mHz to 1 MHz with an amplitude of 10 mV. By using the Zahner Analysis application, all EIS data were fitted and analyzed using model circuits.

In Situ Raman Spectroscopy: The Raman spectra were obtained by using a home-made spectro-electrochemical cell (shown in Figure S8, Supporting Information), which designed for in situ Raman spectroscopy measurement at NCM/ $\text{Li}_6\text{PS}_5\text{Cl}$ interface. The cell was sealed by injecting high-vacuum silicone grease into gaps between the optical window and cell body, and assembled in an Ar-filled glove box before measurement. The Raman spectra in a range of $100\text{--}2500\text{ cm}^{-1}$ were collected using a DXR Raman microscope (Renishaw InVia Raman spectrometer) with He-Ne 532 nm laser excitation and a 50 \times objective. The laser beam with a laser spot size of $\approx 1\text{ }\mu\text{m}$ was focused on each sample and the acquisition time for each spectrum was 20 s. The corresponding optical images were recorded by a Raman microscope.

Other Characterizations: The morphology of samples was observed by SEM (Hitachi S4700). Elemental analysis was conducted on an EDS attached to SEM. XPS measurements were performed on a Thermo ESCALAB 250 system with a monochromatic Al-K α (1486.6 eV) X-ray source to investigate the chemical state of elements. Calibration of the binding energies was conducted relative to the C 1s at 284.8 eV. The XPS data were fitted with the asymmetric Gaussian–Lorentzian sum function in XPSPEAK software.

Supporting Information

Supporting Information is available from the Wiley Online Library or from the author.

Acknowledgements

J.Z. and C.Z. contributed equally to this work. The authors acknowledge the support by Zhejiang Provincial Natural Science Foundation of China

under Grant Nos. LR20E020002, LY17E020010, LY18B030028, and D18E020007, and the National Natural Science Foundation of China (NSFC) under Grant Nos. 21972127, 51677170, 51777194, and 51722210.

Conflict of Interest

The authors declare no conflict of interest.

Keywords

all-solid-state lithium batteries, argyrodite $\text{Li}_6\text{PS}_5\text{Cl}$, in situ characterizations, interface evolution, space charge layer

Received: October 9, 2019
Revised: November 15, 2019
Published online:

- [1] a) P. V. Braun, J. B. Cook, *ACS Nano* **2018**, 12, 3060; b) J. B. Goodenough, Y. Kim, *Chem. Mater.* **2010**, 22, 587; c) J. B. Goodenough, K.-S. Park, *J. Am. Chem. Soc.* **2013**, 135, 1167.
- [2] E. Quartarone, P. Mustarelli, *Chem. Soc. Rev.* **2011**, 40, 2525.
- [3] a) H. Lee, P. Oh, J. Kim, H. Cha, S. Chae, S. Lee, J. Cho, *Adv. Mater.* **2019**, 31, 1900376; b) A. Manthiram, X. Yu, S. Wang, *Nat. Rev. Mater.* **2017**, 2, 16103; c) R. Chen, W. Qu, X. Guo, L. Li, F. Wu, *Mater. Horiz.* **2016**, 3, 487; d) S. Chen, D. Xie, G. Liu, J. P. Mwisizwa, Q. Zhang, Y. Zhao, X. Xu, X. Yao, *Energy Storage Mater.* **2018**, 14, 58.
- [4] Z. Ma, H.-G. Xue, S.-P. Guo, *J. Mater. Sci.* **2018**, 53, 3927.
- [5] a) N. H. H. Phuc, K. Morikawa, T. Mitsuhiro, H. Muto, A. Matsuda, *Ionics* **2017**, 23, 2061; b) H. Yamane, M. Shibata, Y. Shimane, T. Junke, Y. Seino, S. Adams, K. Minami, A. Hayashi, M. Tatsumisago, *Solid State Ionics* **2007**, 178, 1163; c) N. Kamaya, K. Homma, Y. Yamakawa, M. Hirayama, R. Kanno, M. Yonemura, T. Kamiyama, Y. Kato, S. Hama, K. Kawamoto, A. Mitsui, *Nat. Mater.* **2011**, 10, 682.
- [6] a) S. Boulinau, M. Courty, J.-M. Tarascon, V. Viallet, *Solid State Ionics* **2012**, 221, 1; b) Y. Kato, S. Hori, T. Saito, K. Suzuki, M. Hirayama, A. Mitsui, M. Yonemura, H. Iba, R. Kanno, *Nat. Energy* **2016**, 1, 16030; c) E. Rangasamy, Z. Liu, M. Gobet, K. Pilar, G. Sahu, W. Zhou, H. Wu, S. Greenbaum, C. Liang, *J. Am. Chem. Soc.* **2015**, 137, 1384.
- [7] a) H. Morimoto, H. Yamashita, M. Tatsumisago, T. Minami, *J. Am. Ceram. Soc.* **1999**, 82, 1352; b) A. Hayashi, S. Hama, H. Morimoto, M. Tatsumisago, T. Minami, *J. Am. Ceram. Soc.* **2001**, 84, 477.
- [8] a) R. Kanno, T. Hata, Y. Kawamoto, M. Irie, *Solid State Ionics* **2000**, 130, 97; b) Y. Seino, T. Ota, K. Takada, A. Hayashi, M. Tatsumisago, *Energy Environ. Sci.* **2014**, 7, 627; c) G. Sahu, Z. Lin, J. Li, Z. Liu, N. Dudley, C. Liang, *Energy Environ. Sci.* **2014**, 7, 1053.
- [9] Y. Kowada, M. Tatsumisago, T. Minami, H. Adachi, *J. Non-Cryst. Solids* **2008**, 354, 360.
- [10] Ö. U. Kudu, T. Famprikis, B. Fleutot, M.-D. Braidia, T. Le Mercier, M. S. Islam, C. Masquelier, *J. Power Sources* **2018**, 407, 31.
- [11] a) J. Zhang, C. Zheng, J. Lou, Y. Xia, C. Liang, H. Huang, Y. Gan, X. Tao, W. Zhang, *J. Power Sources* **2019**, 412, 78; b) J. Zhang, H. Zhong, C. Zheng, Y. Xia, C. Liang, H. Huang, Y. Gan, X. Tao, W. Zhang, *J. Power Sources* **2018**, 391, 73.
- [12] H.-J. Deiseroth, S.-T. Kong, H. Eckert, J. Vannahme, C. Reiner, T. Zaiß, M. Schlosser, *Angew. Chem.* **2008**, 120, 767.
- [13] M. S. Liao, W. H. E. Schwarz, *Acta Crystallogr., Sect. B: Struct. Sci.* **1994**, 50, 9.
- [14] a) K. Takada, N. Ohta, Y. Tateyama, *J. Inorg. Organomet. Polym. Mater.* **2015**, 25, 205; b) J. Haruyama, K. Sodeyama, L. Han, K. Takada, Y. Tateyama, *Chem. Mater.* **2014**, 26, 4248.
- [15] a) Y. Zhu, X. He, Y. Mo, *J. Mater. Chem. A* **2016**, 4, 3253; b) S. Wenzel, S. Randau, T. Leichtweiß, D. A. Weber, J. Sann, W. G. Zeier, J. Janek, *Chem. Mater.* **2016**, 28, 2400; c) W. D. Richards, L. J. Miara, Y. Wang, J. C. Kim, G. Ceder, *Chem. Mater.* **2016**, 28, 266; d) J. Auvergniot, A. Cassel, J.-B. Ledeuil, V. Viallet, V. Seznec, R. Dedryvère, *Chem. Mater.* **2017**, 29, 3883; e) A. Sakuda, H. Kitaura, A. Hayashi, M. Tatsumisago, Y. Hosoda, T. Nagakane, A. Sakamoto, *Chem. Lett.* **2012**, 41, 260.
- [16] a) M. Nagao, A. Hayashi, M. Tatsumisago, *Electrochem. Commun.* **2012**, 22, 177; b) F. Han, J. Yue, X. Zhu, C. Wang, *Adv. Energy Mater.* **2018**, 8, 1703644.
- [17] a) A. Sakuda, A. Hayashi, M. Tatsumisago, *Sci. Rep.* **2013**, 3, 2261; b) R. Koerver, I. Aygün, T. Leichtweiß, C. Dietrich, W. Zhang, J. O. Binder, P. Hartmann, W. G. Zeier, J. Janek, *Chem. Mater.* **2017**, 29, 5574; c) S. Ohno, R. Koerver, G. Dewald, C. Rosenbach, P. Titscher, D. Steckermeier, A. Kwade, J. Janek, W. G. Zeier, *Chem. Mater.* **2019**, 31, 2930.
- [18] a) L. Sang, R. T. Haasch, A. A. Gewirth, R. G. Nuzzo, *Chem. Mater.* **2017**, 29, 3029; b) R. Koerver, F. Walther, I. Aygün, J. Sann, C. Dietrich, W. G. Zeier, J. Janek, *J. Mater. Chem. A* **2017**, 5, 22750.
- [19] N. Ohta, K. Takada, L. Zhang, R. Ma, M. Osada, T. Sasaki, *Adv. Mater.* **2006**, 18, 2226.
- [20] a) K. Takada, N. Ohta, L. Zhang, K. Fukuda, I. Sakaguchi, R. Ma, M. Osada, T. Sasaki, *Solid State Ionics* **2008**, 179, 1333; b) K. Takada, *Langmuir* **2013**, 29, 7538.
- [21] a) K. Yamamoto, R. Yoshida, T. Sato, H. Matsumoto, H. Kurobe, T. Hamanaka, T. Kato, Y. Iriyama, T. Hirayama, *J. Power Sources* **2014**, 266, 414; b) K. Yamamoto, Y. Iriyama, T. Asaka, T. Hirayama, H. Fujita, C. A. J. Fisher, K. Nonaka, Y. Sugita, Z. Ogumi, *Angew. Chem., Int. Ed.* **2010**, 49, 4414.
- [22] M. Otoyama, Y. Ito, A. Hayashi, M. Tatsumisago, *J. Power Sources* **2016**, 302, 419.
- [23] C. Yu, S. Ganapathy, N. J. J. de Klerk, I. Roslon, E. R. H. van Eck, A. P. M. Kentgens, M. Wagemaker, *J. Am. Chem. Soc.* **2016**, 138, 11192.
- [24] S. Wenzel, S. J. Sedlmaier, C. Dietrich, W. G. Zeier, J. Janek, *Solid State Ionics* **2018**, 318, 102.
- [25] J. Auvergniot, A. Cassel, D. Foix, V. Viallet, V. Seznec, R. Dedryvère, *Solid State Ionics* **2017**, 300, 78.
- [26] J. Kasemchainan, S. Zekoll, D. Spencer Jolly, Z. Ning, G. O. Hartley, J. Marrow, P. G. Bruce, *Nat. Mater.* **2019**, 18, 1105.
- [27] S. Łoś, K. Paprocki, K. Fabisiak, M. Szybowicz, *Carbon* **2019**, 143, 413.
- [28] a) N. Wagner, T. Kaz, K. A. Friedrich, *Electrochim. Acta* **2008**, 53, 7475; b) J. R. Macdonald, L. R. Evangelista, E. K. Lenzi, G. Barbero, *J. Phys. Chem. C* **2011**, 115, 7648; c) S. Hink, N. Wagner, W. G. Bessler, E. Roduner, *Membranes* **2012**, 2, 237.
- [29] J. Lau, R. H. DeBlock, D. M. Butts, D. S. Ashby, C. S. Choi, B. S. Dunn, *Adv. Energy Mater.* **2018**, 8, 1800933.
- [30] a) D. Qu, G. Wang, J. Kafle, J. Harris, L. Crain, Z. Jin, D. Zheng, *Small Methods* **2018**, 2, 1700342; b) D. Jadreško, D. Guziejewski, V. Mirčeski, *ChemElectroChem* **2018**, 5, 187.
- [31] a) K. Tang, X. Yu, J. Sun, H. Li, X. Huang, *Electrochim. Acta* **2011**, 56, 4869; b) G. Du, F. L. Mantia, *ChemElectroChem* **2017**, 4, 122.
- [32] T. Cheng, B. V. Merinov, S. Morozov, W. A. Goddard, *ACS Energy Lett.* **2017**, 2, 1454.
- [33] K. Ohara, A. Mitsui, M. Mori, Y. Onodera, S. Shiotani, Y. Koyama, Y. Orikasa, M. Murakami, K. Shimoda, K. Mori, T. Fukunaga, H. Arai, Y. Uchimoto, Z. Ogumi, *Sci. Rep.* **2016**, 6, 21302.
- [34] T. Hakari, M. Deguchi, K. Mitsuhara, T. Ohta, K. Saito, Y. Orikasa, Y. Uchimoto, Y. Kowada, A. Hayashi, M. Tatsumisago, *Chem. Mater.* **2017**, 29, 4768.
- [35] L. Sang, K. L. Bassett, F. C. Castro, M. J. Young, L. Chen, R. T. Haasch, J. W. Elam, V. P. Dravid, R. G. Nuzzo, A. A. Gewirth, *Chem. Mater.* **2018**, 30, 8747.